

See discussions, stats, and author profiles for this publication at: <https://www.researchgate.net/publication/255954551>

An experimental clinical evaluation of EIT imaging with β_1 data and image norms

Article in *Physiological Measurement* · August 2013

DOI: 10.1088/0967-3334/34/9/1027 · Source: PubMed

CITATIONS

17

READS

89

4 authors:



Yasin Mamatjan

University Health Network

133 PUBLICATIONS 470 CITATIONS

SEE PROFILE



Andrea Borsic

NE Scientific LLC

62 PUBLICATIONS 1,253 CITATIONS

SEE PROFILE



Doga Gursoy

Argonne National Laboratory

73 PUBLICATIONS 878 CITATIONS

SEE PROFILE



Andy Adler

Carleton University

163 PUBLICATIONS 2,786 CITATIONS

SEE PROFILE

Some of the authors of this publication are also working on these related projects:



Characterization of hypoxic tumor microenvironment [View project](#)



Molecular diagnostics [View project](#)

An experimental clinical evaluation of EIT imaging with ℓ_1 data and image norms

This content has been downloaded from IOPscience. Please scroll down to see the full text.

2013 Physiol. Meas. 34 1027

(<http://iopscience.iop.org/0967-3334/34/9/1027>)

View [the table of contents for this issue](#), or go to the [journal homepage](#) for more

Download details:

This content was downloaded by: dogagursoy

IP Address: 146.137.70.71

This content was downloaded on 08/01/2014 at 15:51

Please note that [terms and conditions apply](#).

An experimental clinical evaluation of EIT imaging with ℓ_1 data and image norms

Yasin Mamatjan^{1,2}, Andrea Borsic³, Doga Gürsoy⁴ and Andy Adler¹

¹ Systems and Computer Engineering, Carleton University, Ottawa, Canada

² Electrical-Electronics Engineering, Zirve University, Gaziantep, Turkey

³ Thayer School of Engineering, Dartmouth College, Hanover, NH, USA

⁴ Department of Physics, University of Houston, Houston, TX, USA

E-mail: mamatjan@sce.carleton.ca and adler@sce.carleton.ca

Received 15 March 2013, accepted for publication 3 July 2013

Published 14 August 2013

Online at stacks.iop.org/PM/34/1027

Abstract

Electrical impedance tomography (EIT) produces an image of internal conductivity distributions in a body from current injection and electrical measurements at surface electrodes. Typically, image reconstruction is formulated using regularized schemes in which ℓ_2 -norms are used for both data misfit and image prior terms. Such a formulation is computationally convenient, but favours smooth conductivity solutions and is sensitive to outliers. Recent studies highlighted the potential of ℓ_1 -norm and provided the mathematical basis to improve image quality and robustness of the images to data outliers. In this paper, we (i) extended a primal-dual interior point method (PDIPM) algorithm to 2.5D EIT image reconstruction to solve ℓ_1 and mixed ℓ_1/ℓ_2 formulations efficiently, (ii) evaluated the formulation on clinical and experimental data, and (iii) developed a practical strategy to select hyperparameters using the L-curve which requires minimum user-dependence. The PDIPM algorithm was evaluated using clinical and experimental scenarios on human lung and dog breathing with known electrode errors, which requires a rigorous regularization and causes the failure of reconstruction with an ℓ_2 -norm solution. The results showed that an ℓ_1 solution is not only more robust to unavoidable measurement errors in a clinical setting, but it also provides high contrast resolution on organ boundaries.

Keywords: electrical impedance tomography, Primal Dual Interior Point Method, L1 norm, L2 norm, regularization

(Some figures may appear in colour only in the online journal)

1. Introduction

Electrical impedance tomography (EIT) is a non-invasive and non-ionizing imaging modality that aims to reconstruct the cross-sectional conductivity and permittivity images of a body.

One key area of clinical promise for EIT is in intensive care units (ICUs) by monitoring mechanically ventilated patients. In this application, EIT can resolve changes in the distribution of lung volume as a function of the choice of ventilator settings, and thus to help minimize the risk of lung injury related to the ventilation (Adler *et al* 2012).

Image reconstruction in EIT is an ill-posed inverse problem. The spatial resolution of the reconstructed images is low and limited due to the small number of measurements and underdetermined system of equations. The sensitivity matrix is ill-conditioned and measurement noise usually leads to large artefacts in the images unless regularized appropriately. In order to maintain image stability and meaningful images, regularization techniques are employed to reduce these artefacts. Regularization introduces penalty terms which typically assume smooth conductivity changes that limits reconstruction of sharp images. However, sharp edges are physiologically more realistic corresponding organ boundaries. To reconstruct sharp edges, several techniques have been recently adapted to EIT by recovering discontinuous conductivities using total variation (TV) (Kolehmainen *et al* 1998, Borsic *et al* 2010), and level set methods (Soleimani *et al* 2006, Rahmati *et al* 2012). These approaches have been demonstrated to be useful for solving problems with sharp conductivity transitions.

The inverse problem requires minimization of a cost function which typically consists a data fidelity and a regularization term. Generally, the ℓ_2 -norm is preferred for both terms due to its computational convenience, but results in smooth solutions. The use of ℓ_1 -norm for the regularization is used to preserve edges or promote sparsity and piecewise constant solutions (Rudin *et al* 1992, Chan and Esedoglu 2005). On the other hand, ℓ_1 -norm on the data fidelity term has been referred to as a ‘robust error norm’, and works well when the measurements are contaminated by impulsive noise (Chan *et al* 2010). One recent application of ℓ_1 is for compressive sensing, in which the ℓ_1 -norm (instead of the ℓ_0 -norm) allows improved reconstructions of data from sparse measurements (Donoho 2006).

Preliminary studies for the use of ℓ_1 - and ℓ_2 -norms for the EIT problem based on the lagged diffusivity method (LDM) was conducted using synthetic data (Dai and Adler 2008). They used a weighted identity matrix for regularization which promotes the sparsity, but did not experimentally evaluate the developed algorithms. Additionally, LDMs can only approximate the ℓ_1 solutions due to the presence of a non-differentiable term. To solve this problem efficiently, primal-dual interior point methods (PDIPMs) were developed (Andersen *et al* 2000). Using the PDIPM framework, Borsic and Adler (2012) formulated the ℓ_1 and hybrid ℓ_1/ℓ_2 norm algorithms for inverse reconstruction problems, with a simulation study of EIT as an example.

In this paper, we extended and clinically evaluated PDIPM ℓ_1 and mixed norm image reconstruction algorithms for EIT, and make the following contributions: (1) the image reconstructions framework is elaborated for 2.5D EIT systems, using a coarse-to-fine parameterization (to save memory and computation time) (2) an automatic hyperparameter estimation scheme is developed based on the L-curve approach, and (3) the algorithms are evaluated on simulated and experimental clinical data with a particular focus on the algorithms’ management of measurement errors in our experimental clinical data.

2. Methodology

2.1. EIT inverse problem

A ‘frame’ of EIT measurement data is $\mathbf{y} \in \mathbb{R}^M$, and represents the concatenation surface potentials at the electrodes around the boundary for each applied current pattern. At time

instant t , data \mathbf{y}_t are measured from a medium with a conductivity distribution σ_t . We consider time difference imaging used to produce images of conductivity changes, $\Delta\sigma = \sigma_t - \sigma_0$ between the current time, σ_t , and a previous reference time, σ_0 , due to physiological movement of air and fluid in the body. The conductivity change, $\Delta\sigma$, causes changes in difference EIT measurements $\mathbf{y} = \mathbf{y}_t - \mathbf{y}_0$, where \mathbf{y}_0 is a reference data. Many EIT systems use normalized difference EIT; however, results in this paper are based only on difference EIT. The nonlinear relationship between conductivity change and difference EIT data is represented by a function $f(\cdot)$, as

$$\mathbf{y} = f(\Delta\sigma)|_{\sigma=\sigma_0} = f(\mathbf{P}\mathbf{x})|_{\sigma=\sigma_0} \quad (1)$$

where $f(\cdot)$ is evaluated at the ‘background’ conductivity σ_0 , which is typically considered to be a homogeneous distribution. The 3D conductivity distribution, $\sigma \in \mathbb{R}^{N_\Sigma}$ represents a fine volumetric discretization. This model has a fine discretization especially in regions of high electric field near the electrodes, but is too large for efficient iterative computation of the inverse solution. We thus introduce a coarser model of the conductivity distribution, $\mathbf{x} \in \mathbb{R}^N$ which can be efficiently estimated by our reconstruction algorithm. Here, $\Delta\sigma = \mathbf{P}\mathbf{x}$ using a ‘coarse-to-fine’ mapping, $\mathbf{P} \in \mathbb{R}^{N_\Sigma \times N}$, \mathbf{P} is defined by the geometry of the model and is pre-calculated, such that $[P]_{i,j}$ is a fraction of fine element j inside coarse model element i . In the experimental and simulation examples, we consider a system with electrodes in a horizontal plane. This system represents a ‘2.5D’ system, in which each element of \mathbf{x} represents the conductivity change through a horizontal slice of σ .

The difference EIT system is linearized, such that $\mathbf{y} \approx \mathbf{J}\mathbf{x}$, by the calculation of a Jacobian matrix (or sensitivity matrix) \mathbf{J} where

$$[\mathbf{J}]_{i,j} := \left. \frac{\partial [f(\mathbf{P}\mathbf{x})]_i}{\partial [\mathbf{x}]_j} \right|_{\sigma=\sigma_0} \quad (2)$$

linearizes the model at a background (or reference) conductivity σ_0 . In terms of the fine model, $\mathbf{J} = \mathbf{P}\mathbf{J}_\Sigma$, where \mathbf{J}_Σ is a full Jacobian for fine model σ . In the EIDORS (Adler and Lionheart 2006) software, the $\mathbf{P}\mathbf{J}_\Sigma$ is calculated in one iteration through the coarse elements (size N), by an efficient representation of the adjoint field method (Polydorides and Lionheart 2002).

Generally, the number of unknown model parameters (N) are much more than the available number of data, M , which results in an underdetermined set of equations. The inverse problem for difference EIT of recovering \mathbf{x} from \mathbf{y} based on the linearized sensitivity \mathbf{J} can be stated in the form of a minimization problem as follows:

$$\arg \min_{\mathbf{x}} \left\{ \mathcal{F}(\mathbf{x}) := \|\mathbf{f}(\mathbf{x}) - \mathbf{y}\|_p^p + \|\lambda \mathbf{R}(\mathbf{x} - \mathbf{x}_0)\|_n^n \right\}, \quad (3)$$

where $\|\mathbf{f}(\mathbf{x}) - \mathbf{y}\|_p^p$ is the data fidelity term and $\|\lambda \mathbf{R}(\mathbf{x} - \mathbf{x}_0)\|_n^n$ is the regularization term. \mathbf{x}_0 is the prior estimate of the mean conductivity distribution (which, for difference EIT, set to zero). $\mathbf{R} \in \mathbb{R}^{N \times N}$ is referred to as the regularization matrix and constructed based on a priori information about the model parameters, typically imposing a penalty for large amplitude or non-smooth solutions. The trade-off between these two terms is determined by the hyperparameter λ . p and n specify, respectively, the norms for the data fidelity and regularization terms. The characteristics of the solutions are dependent on the choice of the norms.

2.2. The case for $p = \ell_2$ and $n = \ell_2$

Using ℓ_2 -norm for both data and regularization terms is widely used and the most convenient in terms of computational time and convergence stability. The resultant solutions are commonly referred to as the least-squares solution with Tikhonov regularization.

For linearized difference EIT, $f(\mathbf{x}) \approx \mathbf{J}\mathbf{x}$ and $\mathbf{x}_0 = 0$, and the solution is obtained in one step of the Gauss–Newton method, as:

$$\mathbf{x} = (\mathbf{J}^T \mathbf{J} + \lambda \mathbf{R}^T \mathbf{R})^{-1} \mathbf{J}^T \mathbf{y}. \quad (4)$$

In this case, the ℓ_2 -norm applied on the regularization term acts as a low-pass filter and favours spatially smooth solutions, while ℓ_2 -norm solution for the data term introduces a sensitivity to data outliers (errors), since errors between predicted and actual measurements are squared.

2.3. The case for $p = \ell_2$ and $n = \ell_1$

Using an ℓ_1 -norm instead of ℓ_2 -norm in the regularization term preserves sharp edges in the solutions. For instance, when the regularization matrix is constructed as a gradient operator, the TV norm in the solution are penalized to preserve sharp transitions while overcoming ill-posedness. Such a scheme is referred to as the TV regularization, which is sensitive to the magnitude of changes and preserves the edge information in the restored images. It is particularly attractive for medical applications, because it allows shape reconstruction of sharp transitions at organ boundaries.

The optimal solution can be iteratively obtained by using Newton's method applied to the primal and dual equations with the given complementary condition (details of the derivation of (5) are given in Borsic and Adler (2012)). The dual problems are formulated by introducing two sets of dual parameters, $\mathbf{v} \in R^M$ and $\mathbf{w} \in R^M$ (for $\ell_1 \ell_2$ and $\ell_1 \ell_1$ in later sections). Using Newton's method, the following set of equations is used to calculate the updates, $\Delta \mathbf{x}$ and $\Delta \mathbf{v}$, for \mathbf{x} and \mathbf{v} :

$$\begin{bmatrix} \mathbf{J}^T \mathbf{J} & \lambda \mathbf{R}^T \\ \mathbf{K} \mathbf{R} & -\mathbf{S} \end{bmatrix} \begin{bmatrix} \Delta \mathbf{x} \\ \Delta \mathbf{v} \end{bmatrix} = - \begin{bmatrix} \mathbf{J}^T \boldsymbol{\varepsilon} + \lambda \mathbf{R}^T \mathbf{v} \\ \mathbf{R} \mathbf{x} - \mathbf{S} \mathbf{v} \end{bmatrix} \quad (5)$$

where \mathbf{S} and \mathbf{K} are the diagonal matrices as described follows:

$$\mathbf{S} = \text{diag}(((\mathbf{r}_i \mathbf{x})^2 + \beta)^{1/2}), \quad \mathbf{K} = \text{diag} \left(1 - \frac{v_i \mathbf{r}_i \mathbf{x}}{S_{i,i}} \right). \quad (6)$$

Since the dual update direction given by $\Delta \mathbf{v}$ is not always an ascent direction for the dual function $\mathcal{D}(\mathbf{v})$, we use the *step length rule* to calculate the size of each iterative step, α . The exact step-length (α) is calculated in each iteration (Andersen *et al* 2000) as

$$\alpha = \sup\{\alpha^* : |\mathbf{x}_k + \alpha^* \Delta \mathbf{x}| \leq, i = 1, \dots, n\} \quad (7)$$

where i is the iteration number and α is a scalar value. The approach is applied to calculate the updates of $\Delta \mathbf{x}$, $\Delta \mathbf{w}$ and $\Delta \mathbf{v}$ in each iteration.

The resulting solutions can induce staircase imaging artefacts (Andersen *et al* 2000). The regularization method is slower than linearized Gaussian–Newton method since an iterative method is applied for ℓ_1 -norm solutions of regularization terms that solve larger matrices at each iteration, and it tracks a solution between a primal and dual problem to avoid singularity.

2.4. The case for $p = \ell_1$ and $n = \ell_2$

The ℓ_1 -norm of the data fidelity is much more resilient to outliers than the ℓ_2 -norm since it does not square the measurement misfit (error between the predicted and actual measurements). Thus, it has been preferred to suppress errors originating from outliers (Tarantola 2005). Particularly for EIT, it is attractive because the electrode errors and body motions can induce data outliers and the solutions can easily be spoiled when ℓ_2 -norm is used on the data term.

The following set of equations are used to compute updates, $\Delta \mathbf{x}$ and $\Delta \mathbf{w}$, for \mathbf{x} and \mathbf{w} , respectively:

$$\begin{bmatrix} \lambda \mathbf{R}^T \mathbf{R} & \mathbf{J}^T \\ \mathbf{F} \mathbf{J} & -\mathbf{E} \end{bmatrix} \begin{bmatrix} \Delta \mathbf{x} \\ \Delta \mathbf{w} \end{bmatrix} = - \begin{bmatrix} \mathbf{J}^T \mathbf{w} + \lambda \mathbf{R}^T \mathbf{R} \mathbf{x} \\ \boldsymbol{\varepsilon} - \mathbf{E} \mathbf{w} \end{bmatrix} \quad (8)$$

where \mathbf{E} and \mathbf{F} are the diagonal matrices as described follows,

$$\mathbf{E} = \text{diag}((\varepsilon_i^2 + \beta)^{1/2}), \quad \mathbf{F} = \text{diag}\left(1 - \frac{w_i \varepsilon_i}{E_{i,i}}\right). \quad (9)$$

Again, special attention is needed to obtain the step-length of the dual variable. The resulting solutions are found to be robust to a number of outliers in the data set. This may give an advantage to the ℓ_1 solution in a clinical setting, since it can produce better image quality under higher noise levels and is more robust against measurement outliers, such as those due to movement (Borsic and Adler 2012).

2.5. The case for $p = \ell_1$ and $n = \ell_1$

For this case, the solutions are resilient to data outliers because of the ℓ_1 -norm of the data fidelity term and the ℓ_1 -norm of the regularization term permits reconstruction of sharp edges. However, it is computationally challenging due to the non-differentiability of the absolute value function at a number of points.

According to Newton's equation, the following set of equations are used to compute updates, $\Delta \mathbf{x}$ and the dual variables $\Delta \mathbf{w}$ and $\Delta \mathbf{v}$, for \mathbf{x} , \mathbf{w} and \mathbf{v} , respectively:

$$\begin{bmatrix} 0 & \mathbf{J}^T & \lambda \mathbf{R}^T \\ \mathbf{F} \mathbf{J} & -\mathbf{E} & 0 \\ \mathbf{K} \mathbf{R} & 0 & -\mathbf{S} \end{bmatrix} \begin{bmatrix} \Delta \mathbf{x} \\ \Delta \mathbf{w} \\ \Delta \mathbf{v} \end{bmatrix} = - \begin{bmatrix} \mathbf{J}^T \mathbf{w} + \lambda \mathbf{R}^T \mathbf{v} \\ \boldsymbol{\varepsilon} - \mathbf{E} \mathbf{w} \\ \mathbf{R} \mathbf{x} - \mathbf{S} \mathbf{v} \end{bmatrix} \quad (10)$$

where \mathbf{S} , \mathbf{K} and \mathbf{E} , \mathbf{F} are described in equations (6) and (9), respectively. As in the previous cases, the *step length rule* was utilized for the calculation of the optimal step-length.

2.6. L-curve method

In order to automatically choose the hyperparameter λ , we use the following technique based on the L-curve method (Hansen 1998). The L-curve is a log-log representation of points $(\|f(\mathbf{x}) - \mathbf{y}\|_p, \|\mathbf{R}\mathbf{x}\|_n)$ for each value of λ . It represents the trade-off between data mismatch $(\|f(\mathbf{x}) - \mathbf{y}\|_p)$ as a function of the regularization norm $(\|\mathbf{R}\mathbf{x}\|_n)$. The term 'L-curve' is due to the L-shape with a distinct corner (Hansen 1998). As an example, figure 1 shows the $\ell_2 \ell_2$ norm for simulated data with an added noise (SNR = 40) across the full range of λ values (simulation details are in 2.7).

As shown, for the full range of λ values, the L-curve, in fact, has two corners (with more of a 'chair'-shape). At very low λ , the image norm is unbounded while the data norm is limited by the noise in the data \mathbf{y} . The corner at low λ (the L-curve corner) corresponds to the L-curve recommended λ parameter value. Above this value, the data fit becomes worse, for little improvement in the image norm. At very large values of λ , the best image model is the uniform 'background' conductivity, \mathbf{x}_0 . In this case, the image norm tends to zero, and the L-curve begins to show the 'chair legs' at the bottom right of the figure. The second inflection point does not correspond to any particularly useful value of λ .

For each different ℓ_2/ℓ_1 norm, we first calculate the data misfit and image norm values for the range of parameter values. The corners are calculated by, first, normalizing the log of the norm values to the range between 0 to 1, and adding the two normalized values at each λ . The two L-curve corners are the points of maximum and minimum values on this curve as

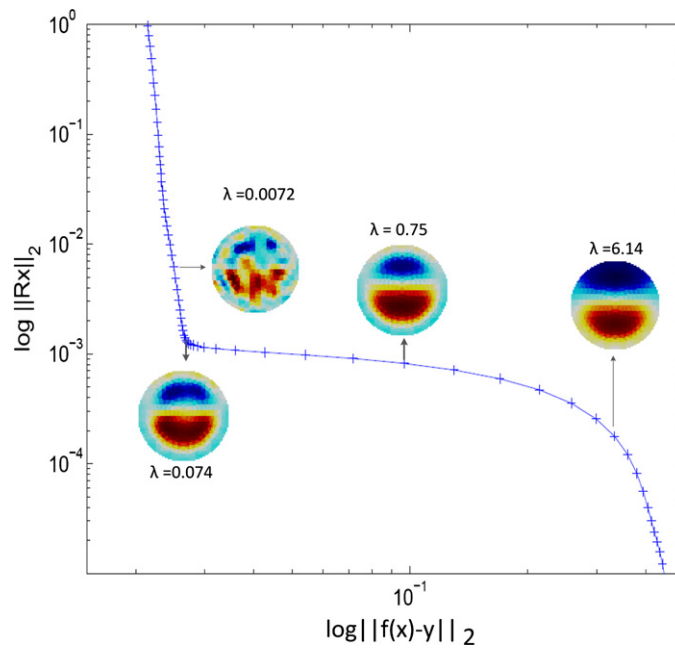


Figure 1. The L-curve for $\ell_2\ell_2$ with $\text{SNR} = 40$. An optimal trade-off between norm estimate and the residual is found at the corner of the first curvature (bottom image).

shown in figure 1. The first L-curve corner point is retained as the choice of hyperparameter. A curve appeared with two distinct corners. Images were reconstructed from a data set by selecting four λ values at the first and second curvatures, as well as the λ at ten higher and ten lower indices at the first curvature. The λ values at the first and second curvatures were estimated from the developed L-curve algorithm. It can be seen from figure 1 that the solution is dominated by the data errors for too little regularization (top left image on the graph), while the solution is not accurate for too much regularization (right image on the graph), since noise as well as useful information are filtered out.

A similar idea commonly underlies $\ell_2\ell_2$ formulations, for instance the local minimum criterion, zero crossing method or balancing principle (Hansen 1998, Clason *et al* 2010). Tehrani *et al* (2012) applied L-curve method to $\ell_2\ell_1$ and showed results based on synthetic data.

2.7. Experimental data

In order to evaluate the developed method, we considered simulated and experimental data from a common EIT configuration, the Sheffield protocol. For most lung imaging, 16 electrodes are arranged on one electrode plane surrounding the medium of interest. Current is injected between each adjacent pair of electrodes while voltages are measured between all other adjacent pairs. Simulations and experimental data were obtained from EIDORS (Adler and Lionheart 2006).

Simulation. The forward model employed in this study was a 3D cylindrical finite element model which was implemented using EIDORS. Figure 2(a) shows a 3D phantom used for generating simulated data (122k elements). The phantom includes two sharp 3D inclusions, where figure 2(b) shows the top view of the phantom with upper and lower regions. The

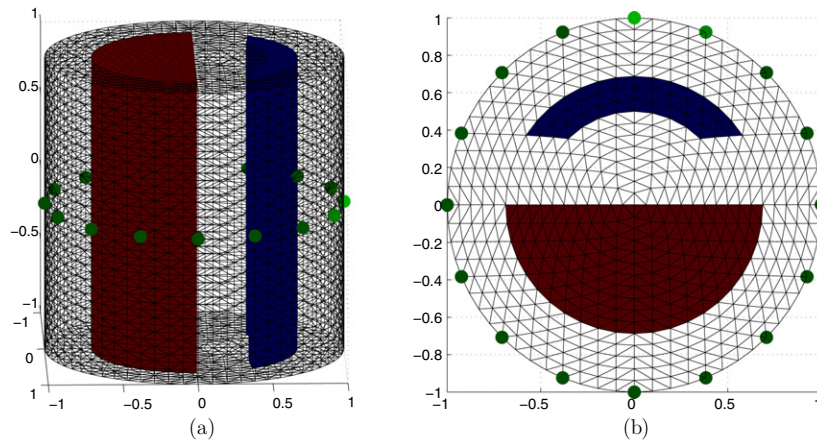


Figure 2. Image of the 3D phantom with two inclusions used for generating the simulated data based on the finite element model. (a) side view, and (b) top view

background conductivity value is 1 S m^{-1} . The top inclusion in figure 2(b) presents a value of 0.5 S m^{-1} and the bottom inclusion has a value of 1.5 S m^{-1} . Electrodes are indicated by green dots around the circular phantom. The reconstructed images are based on a 2D mesh with 576 elements. SNR was defined as the power of the difference signal (\mathbf{y}) to the noise power ratio, where random noise was generated and scaled with the SNR.

A dual model scheme was used in this paper by reconstructing only a 2D slice of a volume, in order to improve memory and computational efficiency compared to 3D image reconstruction. The dual model was implemented by creating a forward model that represents the entire space, and a reconstruction model that represents a cross-section of the volume at a target section of interest. The reconstruction was done by coarse-to-fine mapping, which allows reconstructed images mapped onto any shape of coarse models.

To analyse the performance of the PDIPM framework, the following scenarios were simulated based on: (A) original numerical phantom, (B) added noise which is formed by adding zero mean Gaussian noise to the simulated data to give an SNR of 40, (C) a data error (outlier) as described below, (D) adding noise and a data outlier. Data outliers were introduced as a type of electrode-error to test the robustness of the algorithms for certain electrode malfunction with a measurement failure rate of 0.5% to 24% (1 to 50 measurement indices out of 208 for one frame). The measurement outliers were created by adding 1 (a large value) to the calculated measurement values (with indices 1 to 50) of each EIT data frame based on randomly generated indices (using Matlab `randint` function).

Human data. Experimental data were chosen to reflect practical clinical use of EIT, and the presence of realistic data errors. Data were chosen from a study of intensive care patients in whom the lungs were recruited and ventilator settings were titrated (Gómez-Laberge *et al* 2012). Specifically, paediatric patients with an acute lung injury or acute respiratory distress syndromes (ALI/ARDS) were recruited and EIT was used to monitor their lung mechanics during mechanical ventilation. The experimental protocol consisted of (i) a baseline ventilation stage, (ii) a lung recruitment stage, and (iii) a PEEP (positive end-expiratory pressure) titration stage with sequentially decreased airway pressure. A tidal volume of 6 mL kg^{-1} of body weight was used as baseline ventilation using volume-controlled mode. During the lung ventilation stage, patients were ventilated in pressure-controlled mode with sequentially increased airway pressure. During the PEEP titration stage, the PEEP level

was decreased sequentially to the lowest possible setting, consistent with adequate blood oxygenation. We used the measurement data of patient 7, in which two episodes of electrode errors occur, one during each of the recruitment and titration phases. Further details of patients and lung measurements can be found from Gómez-Laberge *et al* (2012). Measurements were performed with the Goe-MT II EIT device (CareFusion, Hoechberg, Germany) with 16 electrodes in a plane with adjacent stimulation and measurement patterns at a stimulation frequency of 50 kHz.

Dog data: A 16-electrode EIT system was used to take measurements of conductivity changes due to lung ventilation and lung fluid instillation in mongrel dogs (Adler *et al* 1997). Those dogs were anaesthetized and mechanically ventilated. At the same time, three electrocardiography (ECG) electrodes were used to record cardiac activity and synchronized EIT measurements were taken 100 ms after QRS peak of the ECG. Measurements were taken before and after 100 ml of fluids (5% bovine albumin and Evans blue dye) were injected to a lobe of the right lung in the presence of 700 ml inspiration. The same reference data was used before fluid instillation. The mongrel dog with the presence of electrode errors in the measured data was selected for our study.

3. Results

Results were shown first for simulated data in order to validate the technique. Next, results were further demonstrated for a clinical data set with known data outliers. Figure 3 showed the log–log plot of regularization norm versus data mismatch for a wide range of magnitude of λ (from 10^5 to 10^{-12}) for all the ℓ_1 and ℓ_2 combinations of data and regularization terms. Difference signals with six SNR values from 10^5 to 1 were tested to show the effect of different SNR values on the shape of the graphs.

Figure 3 shows a curve with a complex shape that varies as a function of SNR value. The L-curve corner varies with SNR, but the upper portion of the curves (except for the highest SNR) is largely superposed. In both cases with ℓ_2 image norms (figure 3, upper) the L-curve maintains a monotonic shape with λ . However, for the ℓ_1 image norms, there is a brief section in which the image norm decreases below the value it holds in the ‘seat’ region of the ‘chair’. We hypothesize that this behaviour is due to the non-differentiability of the ℓ_1 image parameters. In all cases, the algorithm is able to locate a stable λ parameter value, which provides heuristically satisfactory behaviour.

For all the ℓ_1 and ℓ_2 combinations of data and regularization terms, the solution was not accurate for too much regularization, while the solution was dominated by the data errors for too little regularization. The images lying at the maximum curvature corresponded to an optimal trade-off between norm estimate and the residual. For higher SNR, the curvatures showed smaller data error so less regularization was needed.

Figure 4(a) shows a set of simulated results using the PDIPM algorithm with $\ell_2\ell_2$, $\ell_1\ell_2$, $\ell_2\ell_1$ and $\ell_1\ell_1$ under four test scenarios: (A) without noise in row 1, (B) noise in row 2, (C) 1 outlier in row 3 and (D) both noise (40 SNR) and 1 outlier in row 4. λ was estimated from scenario (A) and fixed for test 1 to test 4 scenarios for all corresponding norms of data and regularization terms. All algorithms provided reasonable reconstructed images for the scenario without noise (row 1), but under noise (row 2), the reconstruction quality dropped for $\ell_1\ell_2$. When an outlier was considered (row 3 and 4), $\ell_2\ell_2$ and $\ell_2\ell_1$ showed large artefacts and did not produce useful images. However, $\ell_1\ell_2$ and $\ell_1\ell_1$ algorithms were still robust with the presence of one data outlier.

Figure 4(b) shows the convergence behaviour of the solutions for a noise-free scenario with a number of iterations: 1 (row 1), 5 (row 2), iteration 10 (row 3), and iteration 15 (row 4).

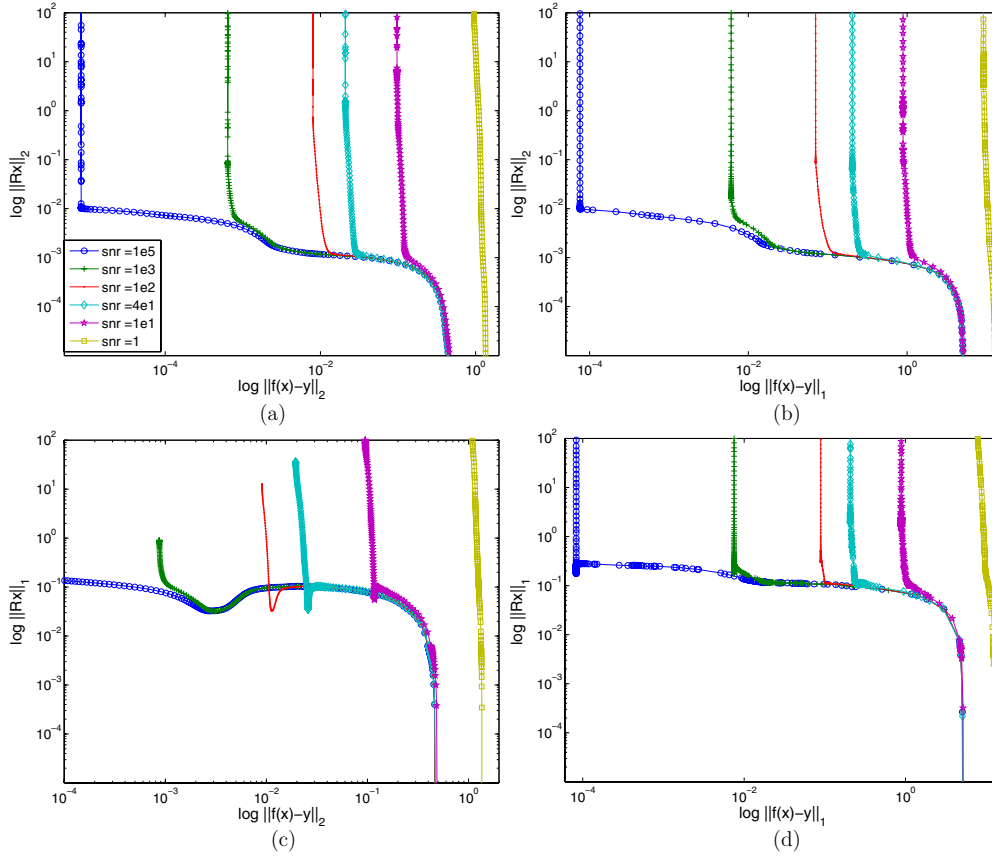


Figure 3. A graph showing the log-log plot of regularization norm versus data mismatch for a fixed large range of magnitude of the regularization with six different SNR values for all the ℓ_1 and ℓ_2 combinations of data and regularization terms such as (a) $\ell_2 \ell_2$, (b) $\ell_1 \ell_2$, (c) $\ell_2 \ell_1$, (d) $\ell_1 \ell_1$.

λ was fixed (based on the estimated values in figure 4(a)) for an increasing number of iterations. The $\ell_2 \ell_2$ algorithm does not require iteration, since we consider a linear inverse problem (thus, all iterations shown are equal). The convergence of $\ell_1 \ell_2$ happened rapidly within 3 iterations. $\ell_1 \ell_1$ converged to a relatively stable solution after 15 iterations. There was no significant reduction in the error after 10 iterations for $\ell_2 \ell_1$. Visually there was little apparent improvement in sample location and dimensions with each iterative step. The computation time (CPU time) for an increasing number of iterations was calculated, where it took 1.4 s for $\ell_1 \ell_2$, 2.3 s for $\ell_2 \ell_1$. $\ell_2 \ell_2$ took the least computation time (0.9 s), while $\ell_1 \ell_1$ took the most computation time (5.7 s) based on the stable solution that they produced.

In order to check which magnitude of data outliers can be acceptable or reduced with PDIPM, a test was undertaken with an increasing number of data outliers (from 1 to 50) by randomly selecting measurement indices and setting them to a large value. The same λ values were used for an increasing number of outliers for $\ell_1 \ell_2$ and $\ell_1 \ell_1$ and five repeated simulations were conducted. The results showed that $\ell_1 \ell_2$ produced good results for an average 27/208 measurement outliers where the range of outliers was 6 to 46. After these numbers of data outliers, the reconstructed images got worse sharply in four tests while gradual distortion happened in one case. $\ell_1 \ell_1$ was found to be more robust against data outliers than $\ell_1 \ell_2$. For

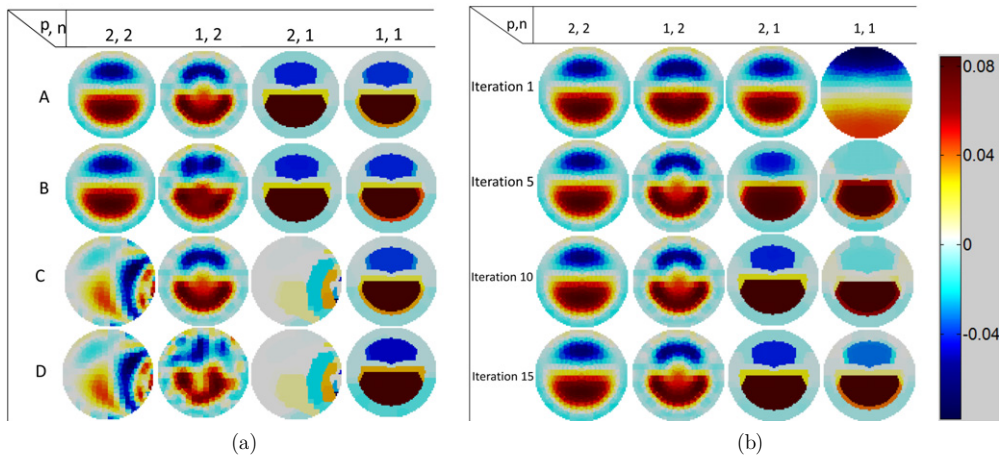


Figure 4. (a) Reconstructed images using PDIPM algorithm with $\ell_2\ell_2$, $\ell_1\ell_2$, $\ell_2\ell_1$ and $\ell_1\ell_1$ under four test scenarios: (A) without noise in row 1, (B) adding noise in row 2, (C) presence of one strong outlier in the dataset in row 3 and (D) both the presence of noise and one strong outlier in row 4. (b) Reconstructed images showing the convergence behaviour of solution under four scenarios for selected numbers of iterations: iteration 1 (row 1), iteration 5 (row 2), iteration 10 (row 3), and iteration 15 (row 4). Note that all iterations shown for $\ell_2\ell_2$ algorithm equals to one (no iteration is required as it is a linear inverse problem).

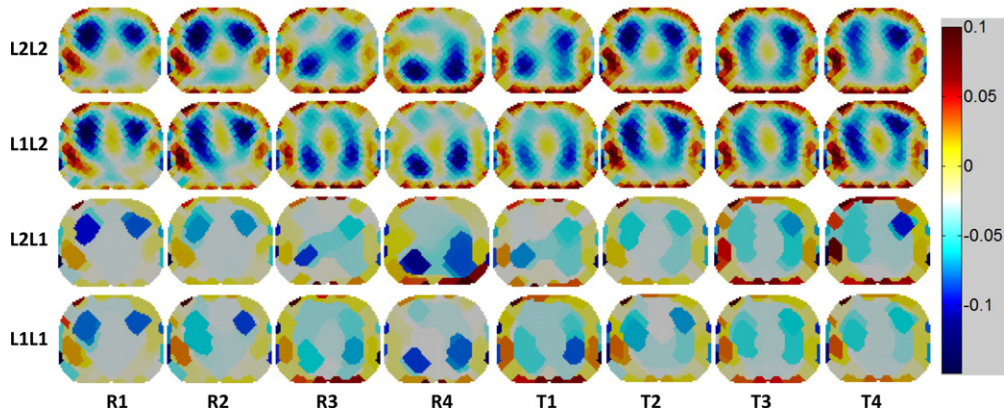


Figure 5. Time difference images of a human thorax for the PDIPM algorithms with four different ℓ -norms on the data and regularization terms. R stands for the lung recruitment and T is for the PEEP titration.

$\ell_1\ell_1$, the distortion appeared to be in two stages: certain shape distortion (average of 23 outliers) and strong artefacts at the edge (average of 40 outliers). The strong artefacts dominated the image, but the shape of the two inclusions was still detected.

Images of experimental EIT data are shown for each clinical phase and algorithm in figure 5. Before the beginning of the protocol, this patient had extensive lung collapse (associated with the ARDS condition), and thus ventilation occurred only in the upper (ventral) region of the lungs. The first four sets of images show the recruitment (R) stage, in which the airway pressure is sequentially increased. This opened the collapsed lung tissue, and moved the ventilation into the lower (dorsal) region.

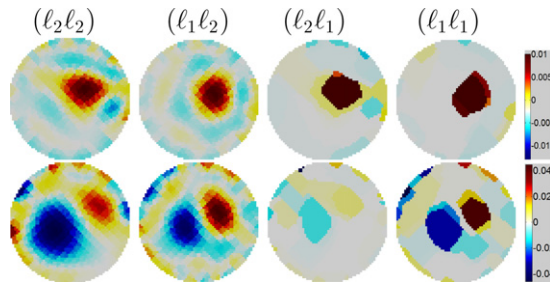


Figure 6. Reconstructed cross-section of conductivity changes in a dog's lung right after injection (row 1) and 60 min after the injection (row 2). Difference images were reconstructed using PDIPM algorithms, where the presence of electrode errors in the measured data affected all reconstructions, except those using the ℓ_1 -norm on the data term (robust reconstruction).

Subsequently, a PEEP titration (T) phase was applied, in which the PEEP value was gradually decreased, in order to attempt to obtain a more uniform pattern of ventilation across the lungs. Except for the images with artefacts (R3 and T1) the images show, for all algorithms, the expected physiological effect. The ventilated region moves downward (dorsally) during phase R, and then upward and more uniformly, during phase T. The algorithms with ℓ_2 image norm, show the expected, slightly blurred, EIT images, while the ℓ_1 image norm shows blocky regions covering the same areas of the thorax. The ℓ_1 image norms generally perform well, and show no large artefact regions. The ℓ_1 and ℓ_2 data misfit norms generate similar images, except for the cases with data errors (R3, T1). Overall, $\ell_1\ell_1$ and $\ell_1\ell_2$ were less affected by the noise, and $\ell_1\ell_1$ produced better localization of centre of ventilation and high spatial resolution.

For these clinical reconstructions, the L-curve graph did not show a suitable first curvature due to large noise levels, and the estimated values were found to be too large, the λ values that produced good reconstructed images were heuristically chosen for the first data set and were fixed for the rest of the data set. We discuss reasons for this behaviour of the L-curve in the discussion section.

Figure 6 illustrates the use of PDIPM algorithms for imaging the conductivity changes in a dog's lung immediately after fluid injection (row 1) and 60 min after the fluid injection (row 2) with the presence of certain level of electrode errors. Row 1 showed the difference images after fluid injection, while row 2 showed the changes of both gas and fluid in the lungs 60 min after the fluid injection. $\ell_2\ell_2$ and $\ell_2\ell_1$ showed a lot of large image artefacts as they suffered from noise from the measurement system. $\ell_1\ell_2$ and $\ell_1\ell_1$ reconstructed cleaner and meaningful images, where particularly $\ell_1\ell_1$ produced sharp images with little image artefacts.

4. Discussions and conclusions

In this study, we expanded the PDIPM framework for EIT inverse problems and evaluated these algorithms in simulation and real-measurement using four combinations of ℓ_1/ℓ_2 norms on data and regularization terms. Comparisons were based on four test scenarios: a numerical phantom, added noise, the presence of one data outlier (error), and added noise and presence of a data outlier. The PDIPM algorithms behaviour was also investigated with retrospective clinical data.

Gauss–Newton based 2-norm solutions have been used frequently as an established traditional method. $\ell_2\ell_2$ basically produces a smooth solution without any clear edge and also it is sensitive to measurement noise (data outliers). ℓ_1 penalty for a data outlier is smaller than ℓ_2 which squared the differences, so ℓ_1 solution is less prone to measurement errors.

The study (figure 4(a)) showed that $\ell_1\ell_2$ and $\ell_1\ell_1$ were not affected by small numbers of data outliers, because of 1-norm for the data term without squared difference between the model and actual data, while $\ell_2\ell_1$ and $\ell_1\ell_1$ produced sharper reconstructed images because of 1-norm on the regularization term which was not overly penalized. $\ell_1\ell_1$ provided both sharp conductivity image and robustness to data outliers.

PDIPM algorithms with 1-norm ($\ell_1\ell_1$) show particular promise in medical applications of EIT, since noise from the acquisition system, and electrode movements or electrode errors are unavoidable, which greatly affect reconstructed image quality based on the 2-norm (data term) solution. However, ℓ_1 solutions are not computationally efficient compared to traditional Gauss–Newton based solutions, since an ℓ_1 solution involves the minimization of a non-differentiable function, and thus requires more computation time and more iterations to reach the convergence.

In a clinical scenario, sharper images are more desirable and data errors are unavoidable due to electrode malfunction or body movement (Asfaw and Adler 2005), while the measurement noise has been modelled as Gaussian to make the statistical computations easier. Hahn *et al* (2008) showed that EIT noise is not Gaussian and varies between channels. To eliminate systematic artefacts, hardware imperfections need to be taken into account by integrating them to the forward model (Hartinger *et al* 2007). While there is no ‘gold standard’ verification on the physiology of the patient, the ℓ_2 -norms (figure 5) showed a physiologically unrealistic scenario, in which the right lung had dorsal ventilation while the left lung was ventrally ventilated. Such a scenario might be possible, but it is physiologically unexpected for this patient’s clinical situation. In contrast, the ℓ_1 -norm images showed reasonable reconstructions, where the reconstructed images of patient’s physiology are realistic and expected. This finding is consistent with an error estimation based on the standard deviation of difference signal, which had three times higher noise levels at R3 and T1 compared to the other experimental phases. We conclude that the unrealistic images from the ℓ_2 -norm are caused by the data errors, and that the ℓ_1 -norm algorithms are more robust and better able to reject data errors (due to electrode malfunction or patient movement).

Hyperparameter values were chosen using the L-curve method which successfully estimated consistent and useful values for the simulation data. The L-curve graph did not show any proper first curvature for large noise levels in real measurements and estimated values that were visually too large. Instead, in figure 5, a range of λ values were tested for the first data set, and the λ values that produced heuristically good reconstructed images were used for the rest of the data set. In simulation, λ values were underestimated for very high or very low SNR i.e. 10^5 or 5 for all the norms of ℓ_1/ℓ_2 , although the L-curve algorithm found a proper curvature. This effect may be explained by the ‘chair’ structure of the L-curve, in which the upper and lower limits join for large noise levels (figure 3).

In the ℓ_1 -based solutions, the ‘staircase effect’ can be observed in the reconstructed images as TV promotes edgy-structures (structures with enhanced edge contrasts) but not sparsity. The ℓ_1 -norm applied to the model parameters promotes sparsity in solutions. However, the TV-functional, which is the ℓ_1 -norm of the gradient of the model parameters, does not promote solution sparsity, but does enhance edgy-structures in reconstructed images.

In summary, we have an extended PDIPM framework with coarse-to-fine mapping for 2.5D image reconstruction, developed an L-curve based scheme to select appropriate parameter values for ℓ_1/ℓ_2 norms, showed potentially significant performance improvements from these approaches in both simulation and clinical study, and made the code publicly available in EIDORS 3.6 under an open source license. These characteristics of $\ell_1\ell_1$ norms demonstrated key advantages of these new approaches such as providing clinically-relevant information

under data errors and reconstructing sharper conductivity profiles (higher contrast resolution) that are closer to the model conductivity distribution.

References

- Adler A, Amyot R, Guardo R, Bates J and Berthiaume Y 1997 Monitoring changes in lung air and liquid volumes with electrical impedance tomography *J. Appl. Physiol.* **83** 1762–7
- Adler A and Lionheart W 2006 Uses and abuses of EIDORS: an extensible software base for EIT *Physiol. Meas.* **27** 25
- Adler A *et al* 2012 Whither lung EIT: where are we, where do we want to go, and what do we need to get there? *Physiol. Meas.* **33** 679–94
- Andersen K, Christiansen E, Conn A and Overton M 2000 An efficient primal-dual interior-point method for minimizing a sum of euclidean norms *SIAM J. Sci. Comput.* **22** 243–62
- Asfaw Y and Adler A 2005 Automatic detection of detached and erroneous electrodes in electrical impedance tomography *Physiol. Meas.* **26** S175–83
- Borsic A and Adler A 2012 A primal dual-interior point framework for using the L1-norm or the L2-norm on the data and regularization terms of inverse problems *Inverse Problems* **28** 27
- Borsic A, Graham B, Adler A and Lionheart W 2010 *In vivo* impedance imaging with total variation regularization *IEEE Trans. Med. Imaging* **29** 44–54
- Chan R, Dong Y and Hintermuller M 2010 An efficient two-phase L1-TV method for restoring blurred images with impulse noise *IEEE Trans. Image Process.* **19** 1731–9
- Chan T and Esedoglu S 2005 Aspects of total variation regularized L1 function approximation *SIAM J. Appl. Math.* **65** 1817–37
- Clason C, Jin B and Kunisch K 2010 A duality-based splitting method for L1-TV image restoration with automatic regularization parameter choice *SIAM J. Sci. Comput.* **32** 1484–505
- Dai T and Adler A 2008 Electrical impedance tomography reconstruction using L1 norms for data and image terms *EMBC'08: 30 Annu. Int. Conf. of IEEE Engineering in Medicine and Biology Society* pp 2721–4
- Donoho D L 2006 Compressed sensing *IEEE Trans. Inform. Theory* **52** 1289–306
- Gómez-Laberge C, Arnold J H and Wolf G 2012 A unified approach for EIT imaging of regional overdistension and atelectasis in acute lung injury *IEEE Trans. Med. Imaging* **31** 834–42
- Hahn G, Just A, Dittmar J and Hellige G 2008 Systematic errors of EIT systems determined by easily-scalable resistive phantoms *Physiol. Meas.* **29** 163–72
- Hansen P 1998 *Rank-Deficient and Discrete ill-Posed Problems: Numerical Aspects of Linear Inversion* (Philadelphia, PA: SIAM)
- Hartinger A, Gagnon H and Guardo R 2007 Accounting for hardware imperfections in EIT image reconstruction algorithms *Physiol. Meas.* **28** 13–27
- Kolehmainen V, Somersalo E, Vauhkonen P, Vauhkonen M and Kaipio J 1998 A bayesian approach and total variation priors in 3D electrical impedance tomography *Proc. 20th Annu. Int. Conf. of IEEE Eng. Med. Biol. Soc.* **vol 2** pp 1028–31
- Polydorides N and Lionheart W 2002 A Matlab toolkit for three-dimensional electrical impedance tomography: a contribution to the electrical impedance and diffuse optical reconstruction software project *Meas. Sci. Technol.* **13** 1871–83
- Rahmati P, Soleimani M, Pullett S, Frerichs I and Adler A 2012 Level-set-based reconstruction algorithm for EIT lung images: first clinical results *Physiol. Meas.* **33** 739–50
- Rudin L I, Osher S J and Fatemi E 1992 Nonlinear total variation based noise removal algorithms *Physica D* **60** 259–68
- Soleimani M, Lionheart W and Dorn O 2006 Level set reconstruction of conductivity and permittivity from boundary electrical measurements using experimental data *Inverse Problems Sci. Eng.* **14** 193–210
- Tarantola A 2005 *Inverse Problem Theory and Methods for Model Parameter Estimation* (Philadelphia, PA: SIAM)
- Tehrani J, McEwan A, Jin C and Schaik A 2012 L1 regularization method in electrical impedance tomography by using the L1-curve (pareto frontier curve) *Appl. Math. Model.* **36** 1095–105